Special Issue paper on Windborne Debris

Effects of wind direction on the flight trajectories of roof sheathing panels under high winds

Bahareh Kordi, Gabriel Traczuk and Gregory A. Kopp*

*Boundary Layer Wind Tunnel Laboratory, Faculty of Engineering,
University of Western Ontario, London, ON, N6A 5B9, Canada*

Abstract. By using the 'failure' model approach, the effects of wind direction on the flight of sheathing panels from the roof of a model house in extreme winds was investigated. A complex relationship between the initial conditions, failure velocities, flight trajectories and speeds was observed. It was found that the local flow field above the roof and in the wake of the house have important effects on the flight of the panels. For example, when the initial panel location is oblique to the wind direction and in the region of separated flow near the roof edge, the panels do not fly from the roof since the resultant aerodynamic forces are small, even though the pressure coefficients at failure are high. For panels that do fly, wake effects from the building are a source of significant variation of flight trajectories and speeds. It was observed that the horizontal velocities of the panels span a range of about 20% – 95% of the roof height gust speed at failure. Numerical calculations assuming uniform, smooth flow appear to be useful for determining panel speeds; in particular, using the mean roof height, 3 sec gust speed provides a useful upper bound for determining panel speeds for the configuration examined. However, there are significant challenges for estimating trajectories using this method.

Keywords: wind borne debris; low-rise buildings; bluff body aerodynamics; hurricanes.

1. Introduction

Roofing materials such as gravel, shingles, tiles, sheathing and structural members (such as 2x4s) are the most common sources of windborne debris. Information pertaining to "how far" and "how fast" windborne debris travels are two of the most important issues to be addressed, since these are directly related to the probability of downstream structures being hit and the probability of failure due to impact when they do hit. Therefore, such information is critical for the development of vulnerability models and appropriate test standards for impact tests. Fig. 1 shows a typical example of flight for a 1.2 m by 1.2 m (4ft by 4ft) plywood sheet, which in this case travelled about 450 m in a downburst in southern Ontario, Canada, illustrating the potential for widespread consequences in suburban neighbourhoods.

Tachikawa's (1983) seminal work has provided the basis for the analysis of plate-like (i.e., shingles, tiles, sheathing) debris. He showed that, in a smooth, uniform flow, different flight patterns

---

* Corresponding Author, E-mail: gakopp@uwo.ca

Fig. 1 Photograph of roof sheathing, caused by a downburst in Bornham, Ontario. The source of the plywood sheathing is the house shown in the background. This particular panel travelled about 450 m

result from different initial angles of attack, and that this could be predicted with quasi-steady models utilizing a combination of static and autorotational force coefficients. He then used these different modes of flight as a means of estimating the variability of flight trajectories in real storms. This basic method has been the common approach used in much subsequent research, including that by Wills, *et al*. (2002), Holmes (2004), Holmes, *et al*. (2006), Lin, *et al*. (2006, 2007), Baker (2007), Richards, *et al*. (2008) and Kordi and Kopp (2009a,b).

However, the "basic approach" presented by Tachikawa (1983) cannot fully help us understand the real situation because it neglects two important facts: (i) windborne debris initiating from a real roof is affected by the building aerodynamics and the local velocities on the roof and in the wake, and (ii) the debris flies in the turbulent wind defined by both the terrain and the gust structure causing failure. While there do not appear to be particular issues with numerical models utilizing the quasi-steady method for debris flight (e.g., Baker 2007; Kordi and Kopp 2009a,b), what is missing is knowledge of the effects of the flow fields in which debris flies. In other words, while we have models for the force coefficients, we do not know the actual aerodynamic forces controlling the flight since we do not have the velocity field that the debris flies in. Therefore, the relation between the uniform flow modelling and actual situations is not clear.

To begin to address this, Visscher and Kopp (2007), using the 'failure' model concept of Surry, *et al*. (2005), examined the flight of aeroelastically-scaled sheathing panels, mounted on the roof of a low-rise building model in a scaled atmospheric boundary layer. They studied the flight of a 1.2 m by 2.4 m (equivalent full-scale) plywood panel from a single location, near the ridge of the leeward roof surface, for one wind direction. Electromagnets were used to provide the equivalent hold down force of the nails. Extending this, Kordi and Kopp (2010), also using the 'failure' model approach, studied the effects of initial conditions on the flight of aeroelastically-scaled roof tiles and asphalt

shingles. In total, they examined 26 different configurations including effects of initial wind direction, location on the roof, hold-down force, and surroundings (including neighbouring structures). These results highlighted the effects of the initial conditions on flight distances and speed, particularly the "local" flow field above the roof in the immediate vicinity of the element. Amongst their findings, they showed that debris "failing" at a higher velocity does not necessarily fly farther – a point which contrasts substantially with uniform, smooth flow results. They also observed that the failures within large separation bubbles do not always lead to flight. In this case, the debris mostly rotates upstream and falls back to the roof because the surface flow around the failed element moves slowly upstream in the separation bubble. However, when the debris element escapes the separation and enters the high speed separated shear layer, it can travel at relatively high elevations, with high speeds. The consequence for shingles is that they have the potential to fly at speeds higher than the undisturbed (i.e., upstream) roof height gust speed. The objective of the current work is to examine the effects of the turbulent flow field above the roof and in the wake on the trajectories and speeds of larger debris, namely, sheathing panels, and to relate this to numerical calculations of the panel flights assuming uniform, smooth flow.

2. Experimental design

2.1. Approach

The failure model approach, described by Surry, *et al.* (2005), and utilized by Visscher and Kopp (2007) and Kordi and Kopp(2010) for debris flight experiments, is used in the present study to examine the trajectory of the sheathing panels originating from a gable roof of a house in a scaled atmospheric boundary layer flow. The current approach is fundamentally different from that of Tachikawa (1983), and subsequently, Lin, *et al.* (2006, 2007), Baker (2007), Richards, *et al.* (2008) and Kordi and Kopp (2009a,b). It is based on defining the problem in terms of the aerodynamics of low-rise buildings, rather than explicitly in terms of the aerodynamics of flat plates in free flight. Focusing on the flight of plates in uniform flow, with an idealized initial condition, likely gives an approximate upper bound on flight speeds and distances, although Kordi and Kopp (2010) showed that this may not always be the case. The current approach, in contrast, defines the problem in the same way as wind loads on low-rise buildings where the building geometry and upstream terrain (and, therefore, wind field) are defined. Since the velocity field above the roof of a low-rise building is more complex than the atmospheric boundary layer, it seems that it will be impractical to determine such velocity fields in detail for a range of buildings. At some point in the future, it may be possible to compute flight trajectories directly, perhaps with large eddy simulations (LES), but in the mean time, more practical methods are required, particularly for loss/risk models such as HAZUS, which consider failure in some detail; but also for debris impact standards that can be based on probabilistic analyses. The current approach provides data that can ultimately be used to calibrate models which possess greater physics, linking failures to debris flight, as well as providing guidance as to which parameters may be critical in modeling.

Details of the experiments are given below. However, it is important to understand that the length scale,

$$\lambda_L = \frac{\text{Length in model scale}}{\text{Length in full scale}} = \frac{1}{20}$$

is chosen, as Visscher and Kopp (2007) point out, as "a compromise between model functionality and a length scale that is suitable for the wind tunnel, with the particular need of having the largest model possible so that the plate dimensions, holding forces, and masses are feasible to construct."

With the length scale set, aeroelastic scaling principles are used to determine model masses, mass-moment-of-inertias, hold down forces, as well as the velocity scale. Froude number scaling is required, so that the effects of gravity are correctly accounted for. This requires matching of the Froude number between model and full scale, i.e.,

$$\sqrt{\frac{U_m^2}{g.L_m}} = \sqrt{\frac{U_f^2}{g.L_f}}$$

where U is a reference velocity, L is a reference length, g is the gravitational acceleration ($= 9.8$ m/s^2), and the subscripts 'm' and 'f' refer to model and full scale, respectively. Therefore, the velocity scale,

$$\lambda_U = \frac{\text{velocity in model scale}}{\text{velocity in full scale}} = \sqrt{\lambda_L} = \sqrt{\frac{1}{20}}$$

Details are given in Table 1, and discussed further below.

Aeroelastic scaling is entirely consistent with the non-dimensional parameters used to define the aerodynamics of flat plates. These parameters are, the Tachikawa number, $Ta = 0.5\rho_{air} \cdot A \cdot U_w^2/(m \cdot g)$, the buoyancy parameter, $\phi = 0.5\rho_{air} \cdot A \cdot l/m$, plate inertia, $\Delta = m \cdot l^2/I$, and the Reynolds number, $Re =$

Table 1 Aeroelastic scaling parameters

Scale	Relationship	Scaling factor
Density scale	$\lambda_\rho = \dfrac{\rho_m}{\rho_f}$	1
Length scale	$\lambda_L = \dfrac{L_m}{L_f}$	$\dfrac{1}{20}$
Velocity scale (Froude)	$\lambda_U = \dfrac{U_m}{U_f} = \sqrt{\lambda_L}$	$\sqrt{\dfrac{1}{20}} = \dfrac{1}{4.472}$
Mass scale	$\lambda_m = \lambda_\rho \cdot \lambda_L^3$	$\dfrac{1}{8000}$
Mass moment of inertia	$\lambda_I = \lambda_m \cdot \lambda_L^2$	$\dfrac{1}{3.2 \times 10^6}$
Time scale	$\lambda_T = \dfrac{T_m}{T_f} = \dfrac{\lambda_L}{\sqrt{\lambda_L}} = \sqrt{\lambda_L}$	$\sqrt{\dfrac{1}{20}} = \dfrac{1}{4.472}$
Force scale	$\lambda_F = \dfrac{F_m}{F_f} = \lambda_\rho \cdot \lambda_U^2 \cdot \lambda_L^2$	$\dfrac{1}{8000}$

$U_w.l/\nu$, where ρ_{air} is the air density, A is the plate area, U_w is the horizontal wind speed, m is the mass of the plate, I is the plate moment of inertia, $m(l^2+h^2)/12$, l is the plate chord, h is the plate thickness, and ν is the kinematic viscosity of air (Baker 2007; Kordi and Kopp 2009b). Baker (2007) non-dimensionalized the spatial coordinates as $\bar{x} = x.\phi/l$ and $\bar{y} = y.\phi/l$ and plate velocities as $\bar{u} = u/U_w$ and $\bar{v} = v/U_w$. We note that the Froude number,

$$Fr = \sqrt{\frac{U_w^2}{g.l}} = \sqrt{\frac{Ta}{\phi}}$$

so that Froude number scaling ensures that Ta, ϕ, and the normalized spatial coordinates are precisely modeled. Therefore, the current parameterization is entirely consistent with that proposed by Baker (2007), which we have also used in our own numerical work (Kordi and Kopp 2009b), and continue to use herein. As is usual in scale model wind tunnel testing for wind effects, Re scaling must be relaxed. It should be noted, however, that the current Re are larger than normal, since the length scale is larger than normal for typical boundary layer wind tunnel experiments.

2.2. House model

As mentioned above, a two-storey, gable roof house at a scale of 1:20 was used for the experiments. This is the same model used by Visscher and Kopp (2007) but is briefly summarized here for completeness. The model has acrylic walls and a roof made of Rohacell 71 modelling foam. The plan dimensions of the model are 0.457 m by 0.519 m, with an eave height of 0.30 m. The gable roof has a pitch of 4:12 and rises 0.09 m from the top of the wall to the ridge. A 0.0254 m roof overhang exists around the perimeter of the building. At a scale of 1:20, the equivalent full-scale dimensions are 9.14 m (30 ft) by 10.38 m (34 ft), with the eave height of 6 m (19.8 ft). Fig. 2 shows a photograph of the model house in the wind tunnel. This is a model of the house being tested at the 'Three Little Pigs' project (Kopp, *et al.* 2008b).

Fig. 2 Photograph of the model house in the wind tunnel, showing the upstream terrain simulation

2.3. Roof sheathing model

The roof sheathing panel dimensions were chosen to match typical dimensions found in practice so that full scale dimensions of 1.2 m by 2.4 m with a thickness of 12.7 mm and mass of 66.9 Kg were considered for the experiment. Note that the mass of the panel assumes that shingles are still attached to the plywood. The mass scale is

$$\lambda_m = \lambda_\rho . \lambda_L^3 = \frac{\text{Mass in model scale}}{\text{Mass in full scale}}$$

where λ_ρ is the density scale. The density scale is 1:1, since air is the common fluid between full scale and the wind tunnel. With the length scale of 1:20, the mass scale is 1:8000. Thus, the model roof sheathing panels were designed to have a length (chord), l, of 60 mm, a width, B, of 120 mm, a thickness of 0.635 mm and a mass of 8.360 gr. The panel was placed with the long edge parallel to the ridge of the roof.

The model sheathing panels were made of Rohacell 71 modelling foam. A thin layer of paint was used on both sides of the panel to help prevent air leakage. To simulate the hold down force of the nails, two circular steel cut-outs were glued on the back of the model panel that would come in contact with the electromagnets located inside the roof cavity. In addition, two longitudinal strips of brass were used on the back of the model to match the required mass-moment-of-inertia about all three axes. Please refer to Fig. 3 of Visscher and Kopp (2007) for a photograph of a typical panel.

2.4. Hold-down force

The scaling relationship for model to full scale forces is

$$\lambda_F = \lambda_\rho . \lambda_U^2 . \lambda_L^2 = \frac{\text{Force in model scale}}{\text{Force in full scale}}$$

Because of the use of Froude scaling, $\lambda_F = (\lambda_L)^3$. Thus, the force scale is 1:8000 in the current experiments.

A total nail pull out resistance, F_l, of 8.54 kN, equivalent to 1.07 N in model scale, was considered for the entire panel. This was comparable to a nailing pattern of 6d nails at 6/12 spacing, obtained from the HAZUS Wind Loss Estimation (Applied Research Associates Inc. 2002). Two electromagnets, located underneath of the model panels inside the roof cavity, were calibrated to provide the appropriate scaled hold-down force. The failure is assumed to occur via wind pressure overcoming the holding force. Thus, the fixture strength integrity, $I'=(F_l+m.g)/(m.g)$, defined by Wills, *et al.* (2002), is 14 in this study.

2.5. Boundary layer simulation

The boundary layer simulation was designed to match an open country terrain, having an aerodynamic roughness length, z_o, of 0.015 m, as defined by Engineering Sciences Data Unit (ESDU 1974, 1982, 1983). The boundary layer was developed using adjustable roughness elements on the wind tunnel floor over the 39 m (128 ft) upstream fetch, 3 large, 1.5 m (59 in) spires, and one 38.5 cm (15 in) high barrier in Boundary Layer Wind Tunnel II at the University of Western Ontario. The obstructions were necessary to generate the large scale turbulent gusts. Since the flow simulation is the

same as Visscher and Kopp (2007), the reader is referred to that work for further details. However, it is emphasized that at a scale of 1:20, the integral scales of the flow are too low compared to actual wind and this may affect the interpretation of the results. In fact, it would be practically impossible to do these experiments with smaller models, which is the reason why we relaxed the scales in the earlier work. This is not expected to substantially alter the aerodynamic loads on the building since the streamwise integral scale, L_x, of 0.91 m is twice the streamwise length of the building (Surry 1982). However, it could have an effect on the interpretation of the trajectory results in equivalent full-scale dimensions, so care needs to be used in such interpretations (although we do present dimensional results in full-scale dimensions, following the practice in the wind engineering discipline).

2.6. Test procedure

Prior to testing, longitudinal and lateral grids, centered 305 mm (1 ft) apart, were laid down on the wind tunnel floor with masking tape. A plastic "bird net" was also tensioned over strips of styrofoam on the floor, spaced longitudinally 914 mm (3 ft) apart, to ease catching the model panel and to minimize its impact with the floor. To capture the trajectory of the panels, one high speed camera was mounted to the ceiling of the wind tunnel to capture the horizontal and lateral movement of the panel and another high speed camera was located beside the model house at almost the same height of the ridge to capture the horizontal and vertical movement of the panel. The position of the side camera can be seen in Fig. 2.

The same procedures as Visscher and Kopp (2007) and Kordi and Kopp (2010) were used for each test. Thus, each test began at a wind velocity that through initial trials was found to have low probability to cause a failure. The duration of each test was equivalent to 10 minutes in full scale, as statistically stationary wind events are typically considered to occur during this duration. This interval is equivalent to 130 sec in model scale. Therefore, during testing, the fan drive voltage would be increased such that the wind tunnel speed is increased by 0.19 m/s (model scale at mean roof height) every 130 sec, unless failure had occurred during the interval.

The failure wind speed measured for each test is based on the wind tunnel fan drive voltage. The failure wind velocity, $\hat{U}_H$, reported herein for each test is an equivalent full-scale, 3-sec gust wind speed at the mean roof height using

$$\hat{U}_H = U_{ref} \times \lambda_U \times \frac{U_H}{U_{ref}} \times \frac{\hat{U}_{3\,\text{sec}}}{\hat{U}_{600\,\text{sec}}} = U_{ref} \times \sqrt{20} \times 0.78 \times \frac{1.52}{1.07} \tag{1}$$

where U_{ref} and U_H are the mean velocities at the reference and mean roof height. The ratio is obtained from the velocity profile measurements in the wind tunnel. $\hat{U}_{3\text{sec}}$ and $\hat{U}_{600\text{sec}}$ are the ratio of 3- and 600-sec gust speeds to the hourly mean wind speed, as obtained by Durst (see ASCE 7-05). It is important to note that it is U_H, the 10-min mean wind speed at the mean roof height in the "undisturbed" boundary layer that is directly measured in the experiments. This is consistent with how loads are measured on low-rise buildings (e.g., Kopp, *et al.* 2005, 2008a), since it is a stable measurement. The use of the peak speed, $\hat{U}_H$, is consistent with the choice of terrain and represents a peak speed that would be associated with building code loads and is entirely consistent with our conversions of wind tunnel pressure data to code-based formulations (e.g., St. Pierre, *et al.* 2005; Kopp, *et al.* 2005).

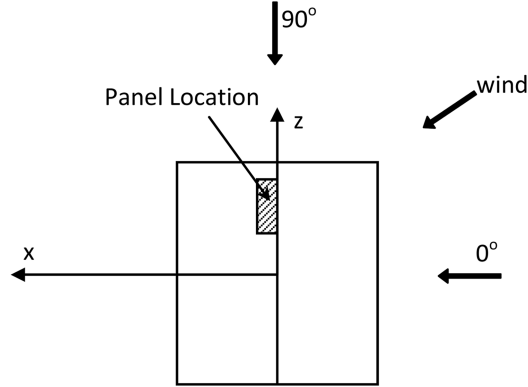It would also be of interest to know the wind speeds above the panel at the moment of failure, but

Fig. 3 Plan view showing the coordinate system, the definition of wind angle, and the plan dimensions of the model house

these have not been measured. Given the high levels of turbulence above the roof, in combination with high spatial gradients (particularly through the separated shear layer), it is not clear what a relevant velocity is for panel flight, although it would be some sort of spatial average. Because of this uncertainty, it seems to be of more practical use to relate the results to U_H or $\hat{U}_H$. We have chosen the latter as a representative gust speed with which to compare panel speeds, and, which is most easily translatable for building codes.

Six wind directions, viz., 15°, 30°, 45°, 60°, 75°, and 90° were examined for one panel location, with about 80 to 100 tests conducted for each wind direction. Fig. 3 shows the location of the panel on the roof of the house with respect to the defined wind directions.

2.7. Calibration and image processing

The longitudinal, vertical, and lateral location of the sheathing panels were captured simultaneously by the two high-speed cameras. A Matlab program was generated to separate the panels (in flight) from the background image and extract the simultaneous longitudinal, vertical, and lateral pixel location of the panel in the images from the two cameras. Since the top camera was placed in the middle of the tunnel, high above the floor, and was pointed parallel to the wind, the longitudinal and lateral, x and z, pixel locations of the panels were estimated from this camera. The grid lines on the floor were used to create a conversion matrix for the (x,z) pixel locations to dimensional values. The heights of the panels, y, were captured by the side camera, but, because of the close proximity and angle of this camera, the estimated vertical locations depend on the (x,z) location. Thus, multiple conversion matrices were created for the side camera by placing a calibration board at several locations in the lateral direction. The calibration matrix closest to the lateral position of the panel was chosen to convert the pixel height to dimensional values. Therefore, the dimensional longitudinal, vertical, and lateral positions as a function of time were obtained for each test.

By using a least squares regression, a polynomial function of time was fit to each set of horizontal, vertical, and lateral locations of the panel trajectory. The impact location of each test was compared with the image processing results and tests with errors lower than 10% on the impact location were considered herein for the panel speed analysis. From the polynomial fit, the longitudinal, u, vertical, v, and lateral, w, velocities of the sheathing panels were obtained by differentiation.

3. Results

3.1. Failure wind speeds

As describe above, U_H and $\hat{U}_H$ are the 10-min (mean) and 3-sec (peak) gust speeds, respectively, at the mean roof height obtained from each test (via Eq. (1)). Then, the means, $(\cdot)_{avg}$, and standard deviations, $(\cdot)_\sigma$, are obtained by averaging all of the individual test results for each configuration. These values are presented in Table 2. It is emphasized again that $\hat{U}_H$ is described by Eq. (1) so that this is not a measured peak speed in the experiment; rather, it is a statistical value using a constant peak factor. The results for the wind direction of 0 degrees, presented in Table 2, are those of Visscher and Kopp (2007) and are included for completeness.

The failure wind speeds of each test were nominally similar for each wind direction, with the ratio of $(\hat{U}_H)_\sigma / (\hat{U}_H)_{avg}$ being less than ~4% for all of the wind directions. In addition, these speeds were observed to fit the Gumbel distribution, as shown in Fig. 4 (for wind directions of 15°, 30°, and 45°). Since the failure load is fixed, the variation is primarily due to the variability in the turbulent gusts which induce the fluctuating wind loads. Since turbulence is a stochastic process, particularly strong gusts may or may not happen during the 10 minute (equivalent full-scale) time increment prior to the next mean wind tunnel speed change. Nevertheless, given the relatively small value of $(\hat{U}_H)_\sigma / (\hat{U}_H)_{avg}$, 10 min (equivalent full-scale) appears to be an appropriate duration to capture the most significant peaks.

Since the panel was located on the roof of the house, the building aerodynamics define the initial conditions at the moment of "failure". By changing the wind direction, the aerodynamic load coefficient, $C_F = (F_I + m.g)/(0.5\rho.\hat{U}_H^2.A)$, varies as represented by the changes in $\hat{U}_H^2$, since $F_I + m.g$ is fixed. Thus, the mean failure wind speeds depend on wind direction. This has a substantial effect, with a range of $(\hat{U}_H)_{avg}$ from 38 m/s for 60° to 56 m/s for 0°. Since the hold down force was kept constant for all tests, the result of the dependence of roof pressure coefficients on wind direction leads to these changing failure wind speeds.

Table 2 Summary of the results (in equivalent full-scale dimensions)

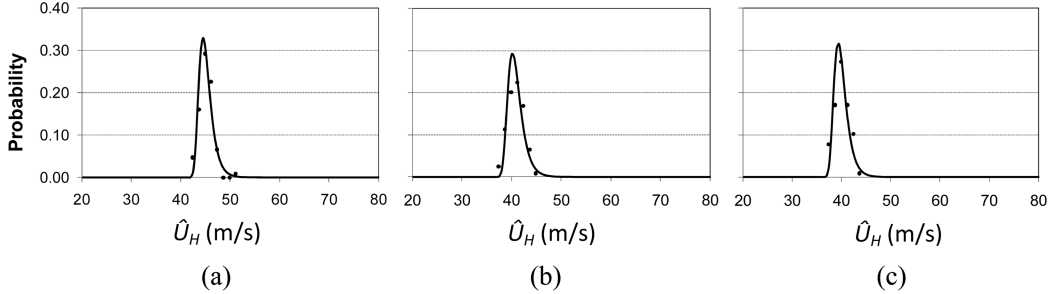| Wind direction	$(U_H)_{avg}$ (m/s)	$(\hat{U}_H)_{avg}$ (m/s)	$(\hat{U}_H)_\sigma$ (m/s)	Impact location (for those that flew, m)				Flight patterns (%)			
				X_{avg}	Z_{avg}	X_σ	Z_σ	Auto-rotational	3D spinning	Translational	No flight
0°	39	56	2.2	33	5	19	5	25	0	75	0
15°	32	45	1.4	36	2	12	5	28	55	17	0
30°	29	41	1.6	43	9	9	3	0	100	0	0
45°	28	40	1.5	31	11	15	4	0	100	0	0
60°	26	38	N/A	13	10	6	4	0	18	0	82
75°	38	53	N/A	-	-	-	-	0	0	0	100
90°	34	48	N/A	-	-	-	-	0	0	0	100

Fig. 4 Distribution of failure velocity, $\hat{U}_H$, for wind directions of (a) 15°, (b) 30°, and (c) 45°

3.2. Flight patterns

Based on the observations from the two high speed cameras located beside and above the house, the observed flight patterns were placed into four categories: auto-rotational, 3D spinning, translational, and no flight. These categories, which are the same as we used in Kordi and Kopp (2010), are defined as:

· Autorotational – The panel rotates about its longer axis, which should remain almost parallel to the z-axis during the flight. This flight pattern is associated with additional lift due to the Magnus effect and is also defined in the literature by Tachikawa (1983), Holmes, *et al*. (2006), and Kordi and Kopp (2009a,b).

· 3D spinning – The panel rotates about different axes, or about any axis other than the "auto-rotational" axis. The rotation about the longer axis when it is not parallel to the z-direction is also in this category. This is the general, six-degree-of-freedom motion.

· Translational - The panel translates in the flow without significant rotation.

· No Flight - The panel stays or lands on the roof immediately after failure.

Table 2 shows the proportion of each observed flight pattern, for each wind direction. For 0°, Visscher and Kopp (2007) observed just two types of flight pattern – autorotational and translational – using Tachikawa's terminology, where the translational mode occurred about three times more often than the autorotational mode for this particular hold down force (or fixture strength integrity). By changing the wind direction from 0° to 15°, the proportion of the autorotational mode remains almost the same, while the number of translational mode flights is reduced. The remainder have shifted to the "3D spinning" mode. This mode is not unexpected since the initial direction of the force on the panel is perpendicular to the surface, by definition, and not aligned with the mean flow direction for this wind angle. This activates all six degrees of freedom, as shown by Richards, *et al*. (2008).

Contrary to what might be expected, the "translational" mode appears to be more sensitive to the out of plane wind direction than the autorotational mode. In any case, for the cornering wind angles like 30° and 45°, 100% of the panels flew in the "3D spinning" mode. Surprisingly, for the wind angles of 60°, 75°, and 90° the panel tends not to fly from the roof. 82% of the panels for the wind direction of 60° and all of the panels with the wind directions of 75° and 90° landed on the roof immediately after failure. The reasons for this will be examined later in the paper.

3.3. Flight trajectory distances

The impact location of each test was obtained by using the two high speed cameras, one mounted on the ceiling and one placed beside the house, as explained in §2. Fig. 5 shows the impact location

of the panels originating from the roof of the house for the wind directions of 0°, 15°, 30°, 45°, and 60°. The averages, X_{avg} and Z_{avg}, and standard deviations, X_σ and Z_σ, of the longitudinal and lateral impact locations, respectively, are also presented in Table 2.

As Fig. 5 shows, the ground impact locations are scattered downstream of the house. For example, for a wind direction of 15°, the panels land between 20-70m downstream of the house, while for 60° they land no further than 25 m downstream. There are several possible reasons for the range of values for both the mean and standard deviation of the flight distances including the variations of the (gust or mean) wind speed at failure, wind turbulence in flight, mode of flight, turbulence and flow structure during the moments surrounding failure, and the angle between the mean wind direction and the normal to the panel.

In terms of mean flight distances, there appear to be, broadly speaking, two groupings. One is for 0° to 45°, where X_{avg} ranges from 31-43m. The second group is for 60° to 90° where X_{avg} ranges from 0-13 m. There are differences in the scatter for all the wind angles examined, but in terms of the mean, this classification seems reasonable. Interestingly, these groups appear to be mostly unrelated to the failure wind speeds, with a range of $(\hat{U}_H)_{avg}$ of 40-56 m/s for the first group and 38-53 m/s for the second. Thus, the use of uniform flow results and models (even with turbulence included) cannot capture this effect without considering, somehow, the effects of initial conditions on the roof and the wake of the house.

The scatter in the impact locations is also critical, because the furthest flight distances give the bounds of risk both in terms of impact locations and speeds. The X_σ results in Table 2 imply that the scatter is greater than what one would expect simply based on the turbulence levels in flight, although this factor undoubtedly contributes some of the scatter. For 0°, with the same panel location, Visscher and Kopp (2007) attributed much of the scatter to the existence of different flight modes. They found that the translational mode spanned a range of 15-40 m, with the autorotational mode spanning 40-110 m for this panel and hold-down condition. However, for 15°, the differences caused by the change of
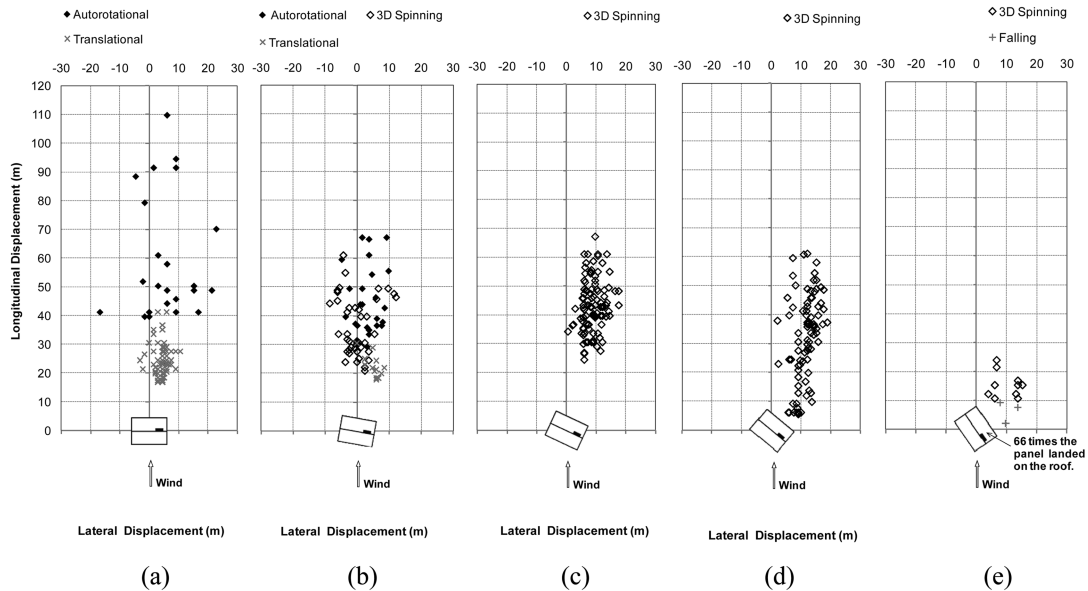

Fig. 5 Measured ground impact locations of the panels for the wind directions of (a) 0°, (b) 15°, (c) 30°, (d) 45°, and (e) 60°. Note that the data for 0° is taken from Visscher and Kopp (2007)

modes are less obvious with little difference between the three modes, as classified. This suggests two things. First, effects of autorotation may only be significant (or, perhaps, dominant) when the wind direction aligns with the normal to the panel, as it does for the current set-up for 0°. Second, for the wind angles examined here (15°-90°), flight mode identification is not really relevant and the panels move with all six degrees of freedom. Additionally, the differences in the scatter for 15° - 60° (since for wind angles greater than 60°, the panel stays on the roof), as observed in Fig. 5, are due to other factors.

Fig. 6 depicts the impact locations as a function of the wind tunnel speed ($\hat{U}_H$). From this figure, it is evident that the variations in the mean wind tunnel speed for the experiments are not a dominant factor affecting the distribution of flight distances. Therefore, this can be largely neglected as a factor contributing to the scatter.

Fig. 7 shows strobe images made from the digital videos for typical examples of the two types of flight for the wind direction of 60°, i.e., one example of 3D spinning and one where the panel did not leave the roof. In this case, the camera was observing the flight from above. From this figure, the role of the wind angle, as it relates to the panel angle, becomes apparent. Because the pressures acts normal to the surface, the initial impulse at failure is also normal to the surface so that initial panel motion is in the direction of the normal to the panel and not in the direction of the wind. Then, for panels which fly, they slowly re-align into the direction of the wind. For 45°, Fig. 5(d) shows that this leads to a scatter
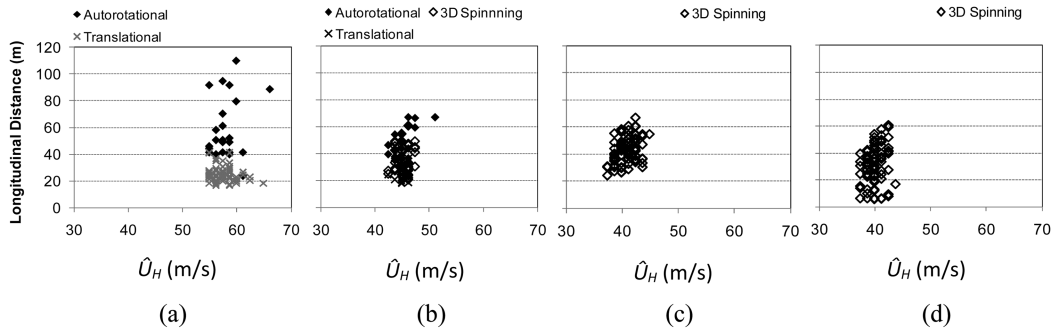

Fig. 6 The longitudinal impact as a function of failure velocity, $\hat{U}_H$, for the wind directions of (a) 0°, (b) 15°, (c) 30°, and (d) 40°. Note that the data for 0° is taken from Visscher and Kopp (2007)
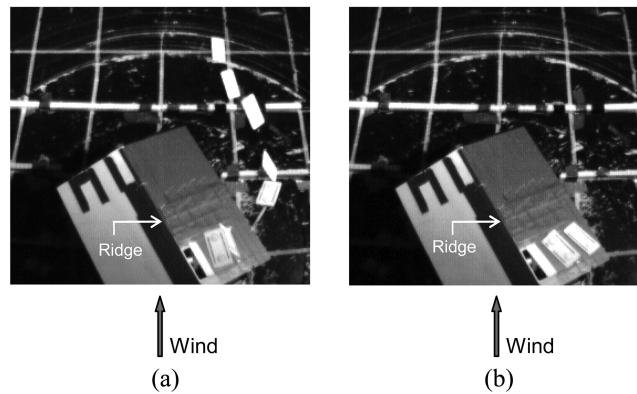

Fig. 7 Strobe images from overhead camera, looking down on the roof, typical of the (a) "3D Spinning" and (b) "no flight" patterns for a wind direction of 60°
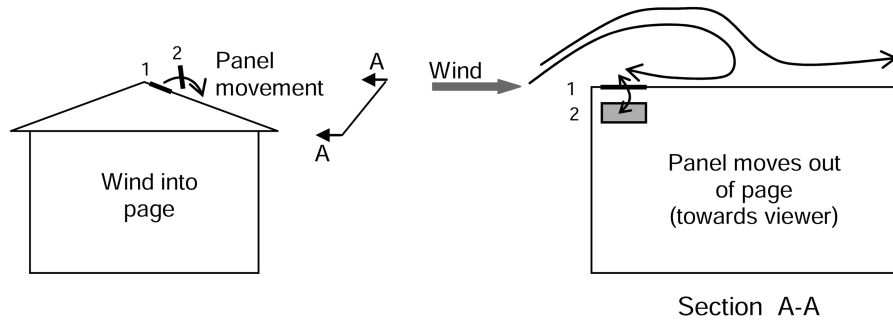
Fig. 8 Failure behaviour and initial movement of the panels, illustrating the flow patterns around the panel for wind directions of 60º, 75º, and 90º

which is primarily in the streamwise (X) direction, with the shortest trajectories ending just downstream of the eaves edges in a straight line on the normal from initial panel location. In contrast the longer flights, land almost straight downstream of this, as the wind direction controls beyond this point.

For 75º and 90º, none of the panels flew; rather, they all landed back on the roof immediately after failure. The panels with the wind direction of 75º either overturned and landed on the roof upside down (like the example for 60º in Fig. 7(b)) or lifted from the long edge close the ridge and dropped back down. For 90º, the panels failed in uplift and subsequently fell back to the roof surface. Fig. 8 is a schematic sketch of the flow field above the panel for the wind directions in the range of 60º - 90º. Examining the elevation view of the gable end, the panel motion is approximately orthogonal to the wind but it stays in the separation bubble generated by the leading edge. This is illustrated in the section view so that the normal to the panel remains orthogonal to the wind when the panel is in position '2'. For this orientation, there is little aerodynamic force on the panel because of its alignment with the direction of flow and the relatively low speed flow near the roof surface in the separation bubble. Thus, the panels are unable to get into the high speed flow to move it downstream and to escape from the roof.

3.4. Flight speeds

The available energy during debris impact is determined by the magnitude of the translational velocity of the object during the flight. With knowledge of debris flight speeds at particular locations, as well as fragility curves for the various wall system components (windows, doors, siding, etc.), the damage potential of the sheathing panels to neighbouring structures could be estimated. The longitudinal, u, vertical, v, and lateral, w, velocities of the sheathing panels were obtained by differentiation of the curve fits to the measured panel trajectories. From these, the magnitude of the resultant translational velocities, $u_{mag}=(u^2+v^2+w^2)^{0.5}$, were also obtained. All the values are non-dimensionalized according to Baker's (2007) formulation: horizontal displacement ($\bar{x} = x \cdot \phi /l$), vertical displacement ($\bar{y} = y \cdot \phi /l$), time ($\bar{t} = t \cdot \hat{U}_H . \phi /l$), horizontal velocity ($\bar{u} = u/\hat{U}_H$), vertical velocity ($\bar{v} = v/\hat{U}_H$), lateral velocity ($\bar{w} = w/\hat{U}_H$), magnitude of translational velocity ($\bar{u}_{mag} = u_{mag}/\hat{U}_H$), as described in §2. The translational speeds of the panels were investigated at two points, viz., eave height (on the way down) and ground level as this gives the range of possible impact speeds with downstream structures. Table 3 gives summary statistics of the non-dimensional speeds for panels at the eave height, $\bar{u}_{mag-eave}$, and at the ground level, $\bar{u}_{mag-ground}$, for wind directions of 15º, 30º, and 45º. The mean and standard deviation are included in the summary. As can be seen,

the average of the translational speeds at the eave height is about 60% of the 3 sec gust speed with the wind direction of 15°, 30°, and 45°. It was also observed that the non-dimensional velocity magnitudes at the eave height and ground level could be fit to lognormal probability distributions (not shown).

Fig. 9 shows the results of $\bar{y}$, $\bar{u}$, $\bar{v}$, and $\bar{w}$ versus $\bar{x}$ for the sheathing panels with the wind directions of 15°, 30°, and 45°. The non-dimensional elevation of the eave and ridge heights are $\bar{y}_{eave} = 0.16$ and $\bar{y}_{eave} = 0.2$, respectively. Note that the non-dimensional horizontal and vertical distances of 1.4 and 0.3, which are limits of the plots, are equivalent to the horizontal and vertical distances of 55 m and 12 m, respectively. Also, note that when the panels flew out of the range of one of the cameras, we were not able to extract the entire trajectory; thus, for those tests, only a portion of the trajectory is presented. From Fig. 9, several observations can be made: (i) The panels initially have a positive vertical velocity and elevate to a height of about 25% above the ridge; (ii) The horizontal velocities of the panels are typically in the range of 20% - 95% of $\hat{U}_H$; (iii) The vertical and lateral panel velocity components are much smaller in magnitude than the horizontal velocity and are mostly less than 30% and 20% of $\hat{U}_H$, respectively.

Table 3 Summary of the impact velocity results

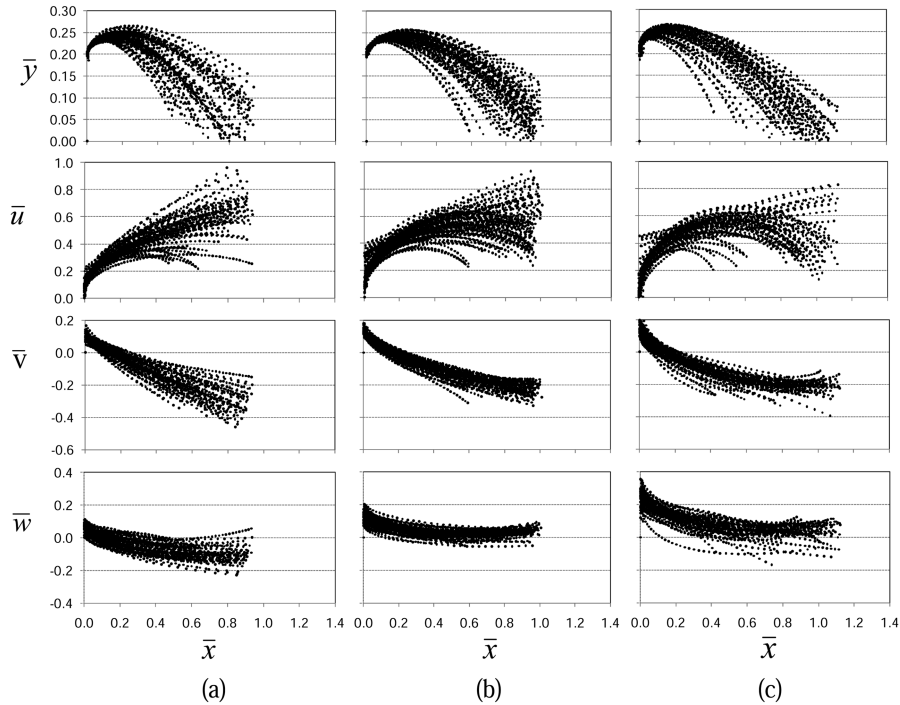| Wind direction	$(\bar{u}_{mag\text{-}eave})_{avg}$	$(\bar{u}_{mag\text{-}eave})_\sigma$	$(\bar{u}_{mag\text{-}ground})_{avg}$	$(\bar{u}_{mag\text{-}ground})_\sigma$
15°	0.58	0.14	0.73	0.21
30°	0.61	0.11	0.58	0.24
45°	0.58	0.08	0.43	0.20

Fig. 9 Non-dimensional trajectories and the corresponding horizontal, vertical, and lateral velocity components of the panels for wind directions of (a) 15°, (b) 30°, and (c) 45°

Wind direction affects the panel flight speeds in complex ways. For 15°, the horizontal speed is observed to (mostly) increase during the flight, with only a few decreasing towards the ground, as can be seen in Fig. 9. In contrast, the horizontal velocity of the panels for 30° and 45° increases only to about $\bar{x} = 0.3$ to 0.5 for all panels, and after that point there are two patterns, either they continue to increase or they decrease. The decreasing speeds may be due to an effect caused by the wake of the house so that the trajectories that are relatively shorter are disproportionately affected by the lower wind speeds in the wake and the panels slow down prior to impact with the ground. In contrast, panels which clear the most significant portion of the wake travel further and have continually increasing speeds, like for panels in a uniform stream.

Fig. 10 shows panel locations in vertical planes 20 and 30 meters downstream of the house which the panels pass through. These planes can be thought of in the following way: If there were a building positioned with one wall, at either $x = 20$ or 30 m, the data shown in the plot represent where the panels would hit on the wall's surface. Data for wind directions of 15° and 30° are presented. As can be seen, the heights of the sheathing panel 'impact' locations are in the range of 3-9 m and 0-7 m vertically, for $x = 20$ and 30 m, while the average heights of the 'impact' locations are 7 and 4.2 m, respectively. Since the eave height of the 'source' building is 6 m, on average, 20 m downstream of the house, the sheathing panels are flying higher than the eave height. By 30 m, they have dropped 40% on average, and it takes up to $x \sim 65$ m for them to all be on the ground, as indicated in Fig. 5. The best fits to the distribution of the vertical positions were found to be Gumbel distributions, as shown in Fig. 11, obtained using the method of moments. In contrast, Tachikawa (1988) found that the best fit was a uniform distribution, using variation obtained from different initial panel angles of attack in uniform flow. This difference may be due to the flow field above the roof and wake effects.

Noting that at $x = 20$ and 30 m downstream of the house, $\bar{x}$ is about 0.5 and 0.75, respectively, it
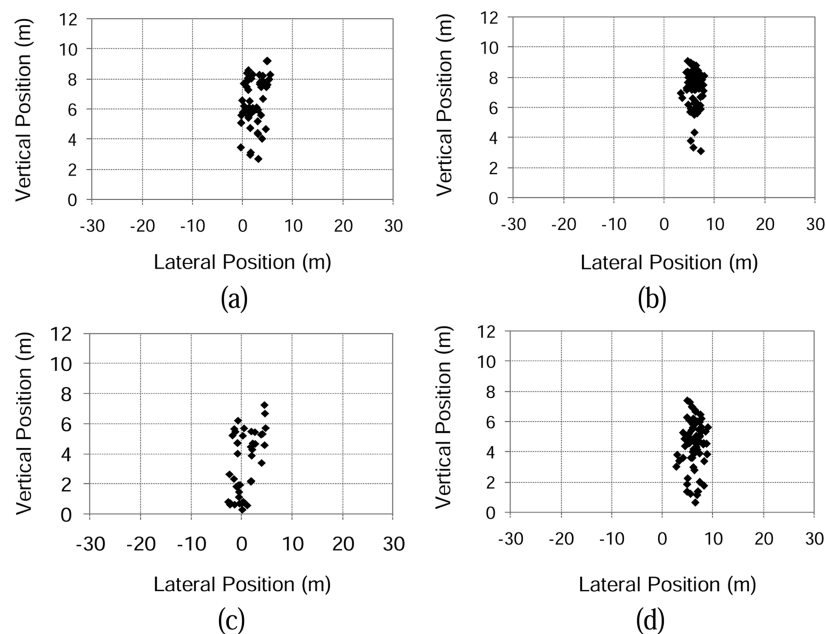

Fig. 10 Vertical planes of sheathing planes flights for the wind directions of (a) 15° and $x = 20$ m, (b) 30° and $x = 20$ m, (c) 15° and $x = 30$ m, and (d) 30° and $x = 30$ m
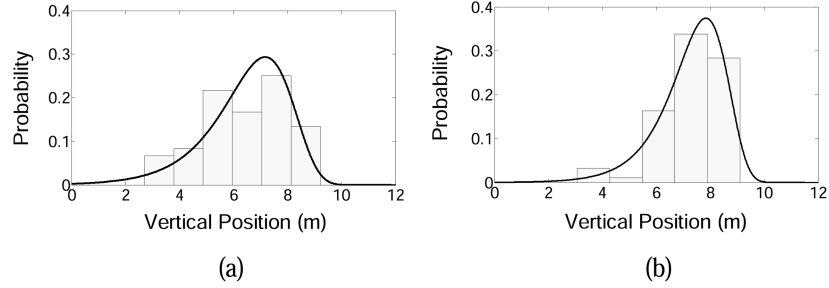
Fig. 11 Distributions of the vertical positions of the panels at $x = 20$ m downstream of the source house for the wind directions of (a) 15° and (b) 30°
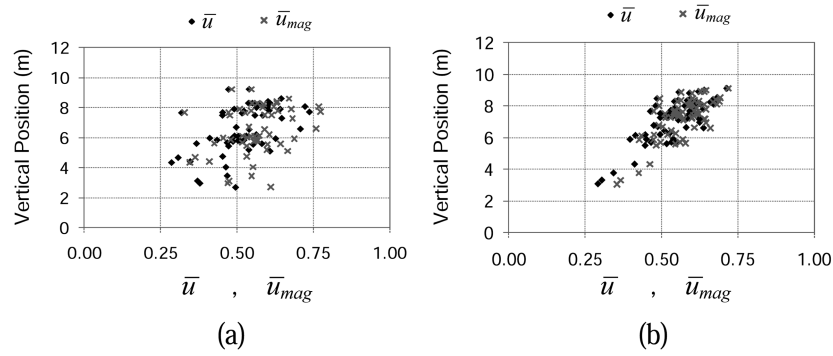

Fig. 12 Panel speeds as a function of vertical positions of the panels at $x = 20$ m downstream of the house for the wind directions of (a) 15°, and (b) 30°

can be observed in Fig. 9 that the non-dimensional horizontal velocities of the panels are in the range of $0.2 - 0.7$ and $0.3 - 0.9$, in the two vertical planes, respectively. Fig. 12 shows the distributions of the panel speeds as a function of height above ground. These data correspond to those in Figs. 10(a) and 10(b). As Fig. 12 shows, there is a slight upward trend of the speeds with height for the wind directions of 15° and noticeable upward trend for the wind direction of 30°. The range of speeds for the bulk of the panels are also higher at $x = 30$ m than at 20 m.

4. Considerations for numerical modelling

Assessing "how far" and "how fast" windborne debris travels is a necessity for risk modeling. Post event damage surveys from hurricanes do not provide any direct information on the speed of debris and provide only limited information regarding how far the debris travels, given the challenges of identifying debris sources, particularly, when wind directions change during a storm. Experiments provide information on both trajectory path and speeds of debris, but it would be impossible to conduct experiments for all possible scenarios. Therefore, the most efficient way to predict variation in debris flight is to have a numerical model that can predict the behaviour with sufficient accuracy, and which has been validated by experimental results.

All of the numerical models presented in the literature for the plate-like debris are based on uniform

smooth flow (e.g., Holmes, *et al.* 2006; Lin, *et al.* 2007; Baker 2007; Richards, *et al.* 2008; Kordi and Kopp, 2009a,b), assuming that the plate travels with the gust that caused failure, and without applying the effects of roof flow fields and building wakes. Numerical solutions are able to provide excellent agreement with available experimental results which were also conducted in a uniform wind flow (Tachikawa 1983; Lin, *et al.* 2006; Kordi and Kopp 2009b). In these experiments, the plates were released into the wind at particular initial angles of attack, without applying the effects of turbulence and initial flow conditions above the roof. Thus, the uniform, smooth flow conditions provide a unique trajectory result for a plate flying in a certain wind speed from a particular initial angle of attack. To explain the variation of trajectories observed in real situations, Tachikawa (1988) attributed the scatter to the different initial angles of attack and found the spatial variation to be uniformly distributed.

Unlike previous experiments, the experimental study presented herein is an attempt to capture the effects of turbulence, the wake generated by the 'source' building, and initial flow conditions on the roof for sheathing panels held down by nails. As such, results from uniform flow simulations have not been compared with this type of experimental data. The purpose of the present section is to make such comparisons.

4.1. Numerical model

The two-dimensional numerical procedure presented in Kordi and Kopp (2009b) is used herein to compare the numerical results with the current experimental results. In the numerical calculations, the static force coefficients are from the data presented by Richards, *et al.* (2008) for plates with aspect ratio, $AR=l/B$, of 2. Thus, the static normal force coefficient, C_N, on the plate is assumed to be

$$C_N = \begin{cases} \dfrac{\alpha}{20^{\circ}} & \alpha \leq 20^{\circ} \\[2mm] 1 - 0.1\dfrac{\alpha - 20^{\circ}}{10^{\circ}} & 20^{\circ} < \alpha \leq 30^{\circ} \\[2mm] 0.9 + 0.2\dfrac{\alpha - 30^{\circ}}{30^{\circ}} & 30^{\circ} < \alpha \leq 60^{\circ} \\[2mm] 1.1 + 0.1\dfrac{\alpha - 60^{\circ}}{30^{\circ}} & 60^{\circ} < \alpha \leq 90^{\circ} \\[2mm] 1.2 - 0.1\dfrac{\alpha - 90^{\circ}}{30^{\circ}} & 90^{\circ} < \alpha \leq 120^{\circ} \\[2mm] 1.1 - 0.2\dfrac{\alpha - 120^{\circ}}{30^{\circ}} & 120^{\circ} < \alpha \leq 150^{\circ} \\[2mm] 0.9 + 0.1\dfrac{\alpha - 150^{\circ}}{10^{\circ}} & 150^{\circ} < \alpha \leq 160^{\circ} \\[2mm] 1 - \dfrac{\alpha - 160^{\circ}}{20^{\circ}} & 160^{\circ} < \alpha \leq 180^{\circ} \end{cases}$$

where α is angle of attack of the relative wind velocity to the plate. The normal force is resolved to yield the static lift, C_{LS}, and drag, C_{DS}, components. An additional drag coefficient of 0.1 is assumed as the effect of the skin friction component (Holmes, *et al.* 2006; Kordi and Kopp 2009b). Thus,

$$C_{LS} = C_N \cos(\alpha)$$

$$C_{DS} = 0.1 + C_N \sin(\alpha)$$

Based on Richards, *et al.*'s (2008) results for the plates with $AR < 4$, the center of pressure, c, is assumed to be at

$$\frac{c}{l} = 0.25 - \frac{\alpha}{2\pi}$$

so that the static moment coefficient, C_{MS}, can be calculated as

$$C_{MS} = \frac{c}{l} \cdot C_N$$

Based on Tachikawa (1983) and Kordi and Kopp (2009b), the rotational drag, C_{DR}, lift, C_{LR}, and moment, C_{MR}, are defined in terms of S/S_0 so that

$$C_{DR} = \begin{cases} 1.16\left|\dfrac{S}{S_0}\right| & \left|\dfrac{S}{S_0}\right| \le 0.4 \\[2ex] 0.465 + 0.108\left(\left|\dfrac{S}{S_0}\right| - 0.4\right) & 0.4 < \left|\dfrac{S}{S_0}\right| < 1 \\[2ex] 0.53 & \left|\dfrac{S}{S_0}\right| \ge 1 \end{cases}$$

$$C_{LR} = \begin{cases} 0.0395 + 0.7505\dfrac{S}{S_0} & 0.6 < \dfrac{S}{S_0} \\[2ex] 0.0727 + 0.6952\dfrac{S}{S_0} & 0.1 \le \dfrac{S}{S_0} \le 0.6 \\[2ex] 1.422\dfrac{S}{S_0} & -0.1 \le \dfrac{S}{S_0} \le 0.1 \\[2ex] -0.0727 + 0.6952\dfrac{S}{S_0} & -0.6 \le \dfrac{S}{S_0} \le -0.1 \\[2ex] -0.0395 + 0.7505\dfrac{S}{S_0} & \dfrac{S}{S_0} < -0.6 \end{cases}$$

$$C_{MR} = \begin{cases} 0.32\left(1 - \dfrac{S}{S_0}\right) & \dfrac{S}{S_0} > 1 \\[2mm] 0.32\left(1 - \left|\dfrac{S}{S_0}\right|\right)\left(\dfrac{S}{S_0}\right) & 0 \le \left|\dfrac{S}{S_0}\right| \le 1 \\[2mm] -0.32\left(1 + \dfrac{S}{S_0}\right) & \dfrac{S}{S_0} < -1 \end{cases}$$

where $S = \omega \cdot l/(2U_{rel})$ is the spin parameter of the plate, ω is the angular velocity of the plate, U_{rel} is the relative wind velocity, $S_0 = \omega_0 \cdot l/(2U_{rel})$ is the spin parameter of the plate at the point of stable autorotation, and ω_0 is the angular velocity of the plate at the point of stable autorotation.

From Iversen (1979), S_0 for a three-dimensional (3D) plate is defined as

$$S_0 = (0.329 \ln \tau^{-1} - 0.0246(\ln \tau^{-1})^2)\left(\left[\frac{AR}{2 + (4 + AR^2)^{\frac{1}{2}}}\right]\left[2 - \left(\frac{AR}{AR + 0.595}\right)^{0.76}\right]\right)^{\frac{2}{3}}$$

where τ is the thickness ratio, h/l.

Therefore, using the numerical procedure described in Kordi and Kopp (2009b) with the force coefficients described above, the non-dimensional asymptotic horizontal velocity for plates with $AR = 2$ is

$$\bar{u}_{asymptotic} = 1 - 0.42\sqrt{\frac{1}{Ta}} \tag{5}$$

where Tachikawa Number, $Ta = (0.5\rho_{air} \cdot A \cdot \hat{U}_H^2)/m \cdot g$, and $\bar{u}_{asymptotic}$ is non-dimensionalized by the 3-sec gust wind speed at the mean roof height, $\hat{U}_H$. Since all of the sheathing panels in the experiments rotate clockwise (for flow from left to right), the associated non-dimensional asymptotic horizontal velocity is considered herein. The Tachikawa number (using $\hat{U}_H$) is in the range of 4.2-5.3 for the panel flights, with the wind directions of 15°, 30°, and 45°; thus, the non-dimensional, asymptotic, horizontal speed of the panels is about 0.8, based on Eq. (5).

4.2. Numerical results and considerations

In Kordi and Kopp (2009b), our numerical model predictions closely matched a range of experimental results in uniform, smooth flow, so the method is helpful for assessing the effects of initial conditions and in-flight velocity fields on the trajectories. Since the majority of the flight patterns observed for panels with the wind directions of 0° and 15° are basically two-dimensional, the results of numerical calculations for these two wind directions are considered herein. Clearly, uniform, smooth flow results are unable to predict the situations where no flight is observed following failure, as occurs for wind directions greater than 60° in the current panel and roof configuration. An initial angle of attack of 20° was applied in the present calculations, close to the value of the roof slope of 18.5°, although the effects of this are examined further below.

The mean values of the 3-sec gust speeds (i.e., failure wind speeds) at the mean roof height for the wind directions of 0° and 15° wind directions are 56 and 45 m/s, respectively. Using these two speeds in the numerical calculations yields ground impact locations of $x = 175$ and 100 m, respectively. These values are much higher than the upper bound of the observed longitudinal impact locations for the wind directions of 0° and 15°, implying that the combination of the effects of initial conditions, boundary layer wind flow, and wake behind the house all reduce the maximum below the uniform, smooth flow result for debris of this size.

Fig. 13(a) shows the numerical results of a panel flying with a speed of 45 m/s along with all of the experimental data for the wind direction of 15°. The end of the numerical curve is impact with the ground. As can be seen, the calculated horizontal panel velocity provides an upper bound to the experimental panel speeds (although a few panels travel faster, perhaps implying higher wind speeds for those cases). This indicates that the assumed 3 sec gust speed represents a practical and reasonable average upper-bound flow speed along these trajectories. However, as Fig. 13(b) shows, the numerical vertical panel velocity is much smaller in magnitude than the experimental vertical velocities, which are negative (i.e., the plates are falling). This is perhaps why the uniform flow calculations over-estimate the impact locations, as compared to the experimental results. As a result, Fig. 13(a) shows that the uniform smooth flow calculations are much better at estimating the upper bound of the debris horizontal speeds than the impact locations.
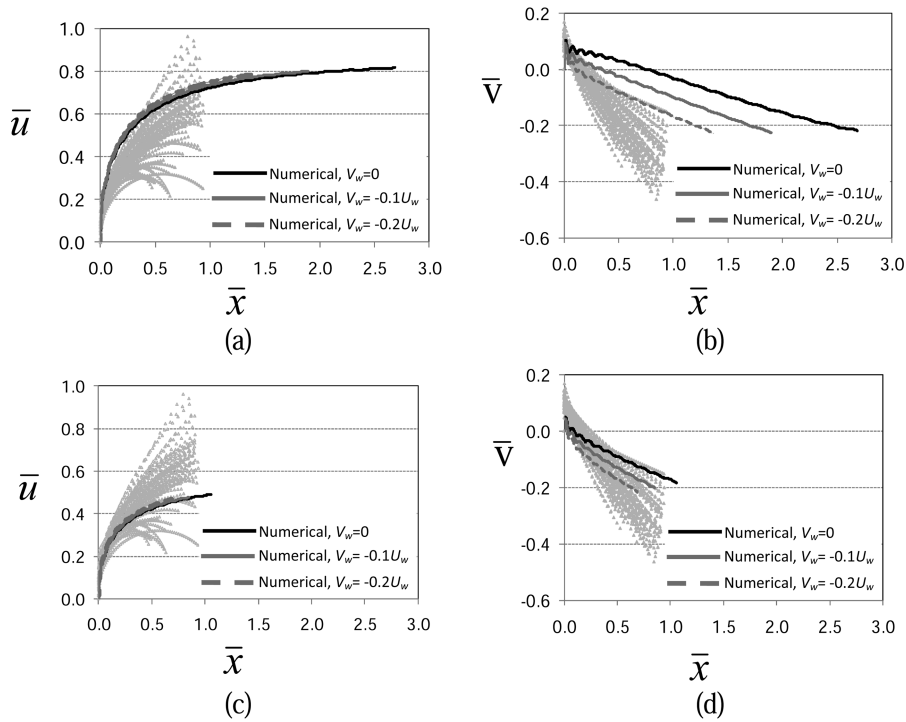

Fig. 13 Non-dimensional horizontal and vertical velocities versus horizontal distance for wind direction of 15°, ▲; (a-b) Non-dimensional horizontal and vertical velocity for a panel flying in a uniform, smooth flow with 3 sec gust speed of 45 m/s and with three downward vertical wind velocities; (c-d) Non-dimensional horizontal and vertical velocity for a panel flying in a uniform, smooth flow with 10-min mean wind speed of 32m/s and with three downward vertical wind velocities

In the real wind flow, the vertical wind velocity, V_w, is not zero along the typical panel trajectories, particularly in the wake of the house, and should be significantly negative as the flow reattaches. However, in the numerical calculations, the vertical wind speed was assumed to be zero, causing the over-estimation of the impact location. Thus, two additional vertical wind speeds were considered. Fig. 13(a) shows the numerical results again using a horizontal wind speed of 45m/s but with two downward vertical wind velocities, namely 10% and 20% of the horizontal wind speed. As expected, the computed vertical velocity of the panel and consequently the impact location are decreased. For instance, the impact locations of the panels flying in winds with speeds of 56 and 45 m/s, with the downward vertical wind speed for 20% of the horizontal wind speed, are decreased to 80m and 55m, respectively.

Following Tachikawa (1988), the effect of initial angle of attack is also examined. Varying the initial angle of attack in the range of $0^o - 55^o$ was found to yield a vertical velocity with the same trend as that of experimental results. The variation in the initial angle of attack mostly affects the vertical panel velocity, consequently changing the impact location. For example, the impact location for the panels travelling with speeds of 56 and 45 m/s, with the initial angle of attack in the range of $0^o - 55^o$, is found to be in the range of 175-120 m and 100-65 m, respectively.

Due to the response time of the panels, as well as effects of the initial flow conditions and the flow field in the wake of the house, it is also possible that the sheathing panels missed the gust and flew in an average wind speed that is substantially lower than the assumed 3-sec gust wind speed. A lower bound of the wind speed, not considering wake effects, would be the mean (10 min) speed. For wind directions of 0° and 15°, the observed 10-min (failure) wind speeds were 39 and 32 m/s, respectively. Using the numerical procedure, the impact locations for the panels with these speeds are 70 and 42 m, respectively. Fig. 13(c) shows the numerical results for a sheathing panel flying in a uniform, smooth 32 m/s wind, along with the experimental results, for the wind direction of 15°. To match the numerical results with the presented experimental results, the numerical translational velocity is non-dimensionalized by the associated 3-sec gust speed, which is 45 m/s in this case. Again, the end of the numerical curve is impact with ground. As can be observed, the numerical horizontal velocity provides something approaching a lower bound to the horizontal velocity data. The numerical results for a panel flying with the 10-min horizontal wind speed and two downward vertical wind velocities, namely, 10% and 20% of the horizontal wind speed, are also shown in Fig. 13(c,d). As shown previously, the computed vertical velocity of the panel and consequently the impact location were decreased. The impact locations of the panels flying in the wind speed of 39 and 32 m/s, with a downward vertical wind speed of 20% of the horizontal wind speed, were decreased to 40 m and 26 m, respectively.

Thus, to obtain the range of the horizontal speed of debris for this particular configuration and wind directions of $0^o - 15^o$, it appears reasonable to use the uniform flow results with horizontal wind speeds in the range from the mean (10 min) to 3 sec gust speed. However, the range of the impact locations is sensitive to the local flow field (above the roof, especially when they do not fly; and wake, when they do fly). It seems unlikely that numerical modelling will be able to successfully model generally the range of trajectories without much greater knowledge of the flow fields around source structures.

5. Conclusions

Wind borne debris has been a significant issue during severe wind storms. The focus of the

current work is on the flight of sheathing panels from the roof of a house in a realistic boundary layer flow with different wind directions. The failure velocity, flight trajectory, and translational velocity were studied in detail. As might be expected, complex relationships between the failure velocity, flight distance, translational velocity, and wind direction were observed. It is concluded that:

· Three-dimensional spinning, with six degrees for freedom, is the most common type of flight patterns observed for the wind directions of 15°, 30°, and 45°. This mode is similar to what Tachikawa (1983) and Visscher and Kopp (2007) labelled as "translational" for their nearly two-dimensional flights. The autorotational mode only appears when the normal to the initial plate location is aligned with the wind direction.

· Almost all of the panels for wind directions of 60° – 90° landed on the roof immediately following "failure". This is because (i) the normal to initial panel location is perpendicular to the wind direction so that initial panel motion is also perpendicular to the wind, and (ii) these panels are located in the low speed region of the separated vortex on the roof and the direction and magnitude of wind speed does not provide significant aerodynamic force to the panels.

· Panels with shorter trajectories, but which fly from the roof, are caught in the wake of the house so that the horizontal and net panel speed is dropping towards impact with the ground. Otherwise, they continue to increase all the way to impact.

· Typical flight speed for panels range between 20% - 95% of the of the estimated roof height gust speed at failure. An upper bound, that envelopes most of the panel flights, is well represented by the asymptotic limit of the panel speed, using the 3 sec gust as the horizontal wind speed.

· The positions of the panels passing through two vertical planes downstream of the house were found to fit the Gumbel distribution, skewed to the high side. However, the associated distribution of the panel speeds was found to increase or slightly increase with height, depending on the wind direction.

· In all tests, the panels are observed to travel on shorter trajectories compared to those estimated by uniform, smooth flow computations with similar 3-sec gust speeds. However, the uniform smooth flow calculations appear to be useful for determining panel speeds. It appears from the numerical analysis that the average horizontal wind speeds along the panel trajectories is in range from the 10-min mean wind speed to the 3-sec gust speed at the mean roof height. It was also observed that the addition of a downward vertical wind speed of about 20% of the horizontal wind speed to the numerical calculations improves the numerical predictions of the trajectory length for the particular panel location investigated here.

References

Applied Research Associates, Inc. (2002), HAZUS, *Wind Loss Estimation Methodology*, Volume I. North Carolina,

October 2002.

ASCE 7-05 (2005), *Minimum Design Loads for Buildings and Other Structures*, American Society of Civil Engineers, Reston, Virginia.

Baker, C.J. (2007), "The debris flight equations", *J. Wind Eng. Ind. Aerod.*, **95**, 329-353.

Engineering Sciences Data Unit (1974), *Characteristics of atmospheric turbulence near the ground*, Data Item 74031.

Engineering Sciences Data Unit (1982), *Strong winds in the atmosphere boundary layer. Part 1: Mean-hourly wind speeds*, Data Item 82026.

Engineering Sciences Data Unit (1983), *Strong winds in the atmosphere boundary layer. Part 2: Discrete gust speeds*, Data Item 83045.

Holmes, J.D. (2004), "Trajectories of spheres in strong winds with application to wind-borne debris", *J. Wind Eng. Ind. Aerod.*, **92**, 9-22.

Holmes, J.D., Letchford, C.W. and Lin, N. (2006), "Investigations of plate-type windborne debris- Part II :Computed trajectories", *J. Wind Eng. Ind. Aerod.*, **94**, 21-39.

Iversen, J.D. (1979), "Autorotating flat plate wings: the effect of the moment of inertia, geometry and Reynolds number", *J. Fluid Mech.*, **92**, 327-348.

Kopp, G.A., Surry, D. and Mans, C. (2005), "Wind effects of parapets on low buildings: Part 1. Basic aerodynamics and local loads", *J. Wind Eng. Ind. Aerod.*, **93**, 817-841.

Kopp, G.A., Oh, J.H. and Inculet, D.R. (2008a), "Wind-induced internal pressures in houses", *J. Struct. Eng.* ASCE, **134**, 1129-1138.

Kopp, G.A., Morrison, M.J., Iizumi, E., Henderson, D. and Hong, H.P. (2008b), "The 'Three Little Pigs' Project: Hurricane Risk Mitigation by Integrated Wind Tunnel and Full-Scale Laboratory Tests", *Nat. Hazards Review*, ASCE, (submitted).

Kordi, B. and Kopp, G.A. (2009a), "Discussion of the debris flight equations", *J. Wind Eng. Ind. Aerod.*, **97**, 151-154.

Kordi, B. and Kopp, G.A. (2009b), "Evaluation of the quasi-steady theory applied to windborne flat plates in uniform flow", *J. Eng. Mech.* ASCE, **135**(7), 657-668.

Kordi, B. and Kopp, G.A. (2010), "Effects of Initial Conditions on the Flight of Windborne Plate Debris", *J. Wind Eng. Ind. Aerod.*, (submitted).

Lin, N., Letchford, C. and Holmes, J.D. (2006), "Investigation of plate-type windborne debris. Part I. Experiments in wind tunnel and full scale", *J. Wind Eng. Ind. Aerod.*, **94**, 51-76.

Lin, N., Holmes, J.D. and Letchford, C. (2007), "Trajectories of Wind-Borne Debris in Horizontal Winds and Applications to Impact Testing", *J. Struct. Eng.* ASCE, **133**, 274-282.

Richards, P.J., Williams, N., Laing, B., McCarty, M. and Pond, M. (2008), "Numerical calculation of the threedimensional motion of wind-borne debris", *J. Wind Eng. Ind. Aerod.*, **96**, 2188-2202.

St. Pierre, L.M., Kopp, G.A., Surry, D. and Ho, T.C.E. (2005), "The UWO contribution to the NIST aerodynamic database for wind loads on low buildings: Part 2. Comparison of data with wind load provisions", *J. Wind Eng. Ind. Aerod.*, **93**, 31-59.

Surry, D. (1982), *Consequences of distortions in the flow including mismatching scales and intensities of turbulence*, Wind Tunnel modelling for civil engineering applications, (ED: T.A. Reinhold), Cambridge University Press, Cambridge, 1982, 137-185.

Surry, D., Kopp, G.A. and Bartlett, F.M. (2005), "Wind load testing of low buildings to failure at model and full scale", *Nat. Hazards Review*, ASCE, **6**, 121-128.

Tachikawa, M. (1983), "Trajectories of flat plates in uniform flow with application to wind-generated missiles", *J. Wind Eng. Ind. Aerod.*, **14**, 443-453.

Tachikawa, M. (1988), "A method for estimating the distribution range of trajectories of wind-borne missiles", *J. Wind Eng. Ind. Aerod.*, **29**, 175-184.

Visscher, B.T. and Kopp, G.A. (2007), "Trajectories of roof sheathing panels under high winds", *J. Wind Eng. Ind. Aerod.*, **95**, 697-713.

Wills, J.A.B., Lee, B.E. and Wyatt, T.A. (2002), "A model of wind-borne debris damage", *J. Wind Eng. Ind. Aerod.*, **90**, 555-565.